

# Interpretation of measurements of the number of muons in extensive air shower experiments



Raul R. Prado<sup>a,\*</sup>, Ruben Conceição<sup>b</sup>, Mário Pimenta<sup>b</sup>, Vitor de Souza<sup>a</sup>

<sup>a</sup>Instituto de Física de São Carlos, Universidade de São Paulo, São Carlos, Brazil

<sup>b</sup>Laboratório de Instrumentação e Física Experimental de Partículas, Lisbon, Portugal

## ARTICLE INFO

### Article history:

Received 25 January 2016

Revised 8 June 2016

Accepted 19 July 2016

Available online 20 July 2016

### Keywords:

Ultra high energy cosmic rays

Muons

Composition

## ABSTRACT

In this paper we analyze the energy evolution of the muon content of air showers between  $10^{18.4}$  and  $10^{19.6}$  eV to be able to determine the most likely mass composition scenario from future number of muons measurements. The energy and primary mass evolution of the number of muons is studied based on the Heitler–Matthews model and Monte Carlo simulation of the air shower. A simple model to describe the evolution of the first and second moments of number of muons distributions is proposed and validated. An analysis approach based on the comparison between this model's predictions and data to discriminate among a set of composition scenarios is presented and tested with simulations. It is shown that the composition scenarios can be potentially discriminated under the conditions imposed by the method. The discrimination power of the proposed analysis is stable under systematic changes of the absolute number of muons from model predictions and on the scale of the reconstructed energy.

© 2016 Elsevier B.V. All rights reserved.

## 1. Introduction

The energy spectrum of ultra high energy cosmic rays (UHECRs) has been measured recently with high precision and two major features were confirmed. The ankle ( $\log(E/\text{eV}) \sim 18.7$ ) and the flux suppression ( $\log(E/\text{eV}) \sim 19.5$ ) have been undoubtedly established by HiRes [1], the Pierre Auger Observatory [2,3] and Telescope Array [4]. However, the astrophysical interpretation of these structures cannot be inferred with complete certainty mainly because of the lack of knowledge on the UHECR composition at these energies. In a light abundance scenario, the ankle could be interpreted as the modulation resulting from the particle interaction with radiation backgrounds [5,6]. On the other hand, it could also be explained as the transition from galactic to extra-galactic cosmic rays [7]. The flux suppression can be equally well described by the energy losses of extra-galactic particles due to interactions with CMB photons [8] or by the maximum reachable energy of the astrophysical acceleration mechanisms in nearby sources [9]. In each one of these astrophysical scenarios, the energy evolution of the UHECR composition is significantly different.

The UHECR measurements are done indirectly through the detection of extensive air showers. Therefore, the determination of

the composition depends strongly on the data analysis capability to correlate the measured properties of the shower to the primary particle type. This correlation is achieved using air shower simulations. However, intrinsic fluctuations of the showers and uncertainties in the high energy hadronic interaction models for energies above  $10^{17}$  eV prevent us from a definitive conclusion about the primary particle type for each event. Statistical analysis and evolution trends [10,11] are used to minimize the fluctuation effects, nevertheless a unique interpretation of the data is not possible because of the hadronic interaction model uncertainties. Currently, the most reliable observable to investigate composition at higher energies is  $X_{\text{max}}$ , the atmospheric depth at which the shower reaches the maximum number of particles [12]. A second very powerful observable sensitive to primary particle mass is the number of muons ( $N_{\mu}$ ) in the showers. However, the lack of knowledge of the high energy hadronic interactions and the systematic uncertainties in the energy determination limit the interpretation of  $N_{\mu}$  data in terms of composition in a more severe way than they do for  $X_{\text{max}}$ . There are several indications that the current most often used hadronic interaction models fail at predicting the muonic component features of air showers [13,14]. Moreover, as  $N_{\mu}$  scales directly with shower energy, the systematic uncertainty in energy reconstruction (typically  $\sim 10 - 20\%$ ) represents also a difficult challenge to overcome in the interpretation of the  $N_{\mu}$  data. As a consequence, it is not straightforward to envisage a data analysis procedure that extracts the mass abundance from the  $N_{\mu}$  data.

\* Corresponding author.

E-mail address: [raul.prado@usp.br](mailto:raul.prado@usp.br) (R. R. Prado).

In this paper we propose a new approach to interpret  $N_\mu$  data which accommodates the systematic uncertainties of the high energy hadronic interaction models and of the energy reconstruction. The analysis proposed here is based on the energy evolution of the first ( $\langle \log_{10} N_\mu \rangle$ ) and second ( $\sigma[\log_{10} N_\mu]$ ) moments of the  $\log_{10} N_\mu$  distribution. There are two central features of the proposed procedure: (a) a simplified model to describe the energy and mass evolution of  $\langle \log_{10} N_\mu \rangle$  and  $\sigma[\log_{10} N_\mu]$  which minimizes the hadronic interaction model dependencies, and (b) a comparison between the predictions of this model for a set of given composition scenarios and the data integrated in energy to maximize the discrimination power.

First in Section 2 we propose a simplified model to describe the energy and mass evolution of  $\langle \log_{10} N_\mu \rangle$  and  $\sigma[\log_{10} N_\mu]$ . We argue that to a very good approximation only two parameters ( $a$  and  $b$ ) summarize all uncertainties of the currently used high energy hadronic interaction models. This simplification of the description of  $\langle \log_{10} N_\mu \rangle$  and  $\sigma[\log_{10} N_\mu]$  with energy and mass is an important step in the analysis procedure because it minimizes the dependencies on hadronic interaction models in the interpretation of the data. In Section 3.1 we use shower simulations to study the energy and mass evolution of  $\langle \log_{10} N_\mu \rangle$  and  $\sigma[\log_{10} N_\mu]$  and to validate the model proposed in Section 2. We also introduce in Section 3.1 the algorithm developed to build the large set of simulations used in this paper. This simulation process is complemented in Appendix A.

In Section 4 we introduce a set of six benchmark composition scenarios defined by the percentage of proton, helium, nitrogen and iron nuclei as a function of energy. Four composition scenarios are astrophysical motivated (based in Refs. [6–9,15]) and two were derived from the  $X_{\max}$  measurements performed by the Pierre Auger Collaboration (based on Ref. [16]). By using simulations we also study the energy evolution of  $\langle \log_{10} N_\mu \rangle$  and  $\sigma[\log_{10} N_\mu]$  for each one of these scenarios and evaluate the effects of the uncertainties on the energy scale and on the absolute  $N_\mu$  due to the misprediction by the hadronic interaction models.

In Section 5 we show how the model proposed in Section 2 can be used to discriminate between these representative composition scenarios. The comparison of the model predictions for the composition scenarios with the data in an energy range is the important step of the analysis procedure proposed here because it maximizes the discrimination power allowing us to identify the most likely scenario that generated a set of  $N_\mu$  data. This comparison is done by the traditional  $\chi^2$ , which assumes the minimal value for the composition scenario which best describes the data. We use simulations to test our approach and show that it is possible to achieve a good discrimination between the chosen scenarios supposing a realistic case with the statistic to be collected during 3 years of data taking with the Pierre Auger Observatory Upgrade - AugerPrime. We also show that the systematic uncertainties in the energy reconstruction and on the absolute scale of the number of muons do not mix the composition scenarios. Hence we conclude in Section 6 that by using only the energy evolution of  $\langle \log_{10} N_\mu \rangle$  and  $\sigma[\log_{10} N_\mu]$  it would be possible to identify, by comparing the composition scenarios to the data, the scenario which best describes the measurements of  $N_\mu$ .

## 2. A model for the energy and mass evolution of $\log_{10} N_\mu$ moments

In this section we present a model to describe the energy and primary mass evolution of the  $\log_{10} N_\mu$  first and second moments. The Heitler–Matthews model [17] is a semi-empirical description of the shower development which describes the dependencies of

the mean  $N_\mu$  as

$$\langle N_\mu \rangle_A = A^{1-\beta} N_\mu^p \quad (1)$$

and

$$\langle N_\mu \rangle_E = \left( \frac{E}{\zeta_c^\pi} \right)^\beta, \quad (2)$$

where  $N_\mu^p$  is the number of muons in a proton shower and  $\zeta_c^\pi$  is the pion critical energy, assumed to be equal to 20 GeV in [17].  $\beta$  is often taken to be constant because its value is shown to vary in a small interval from 0.85 to 0.92 [17,18].

Both equations define a clear linear relation of  $\langle \log_{10} N_\mu \rangle$  with energy and mass that can be summarized as

$$\langle \log_{10} N_\mu \rangle_{E,A} = a + D_A \cdot \ln(A) + D_E \cdot (\log_{10} E - 19.0), \quad (3)$$

where  $D_E = \beta \simeq 0.85 - 0.92$ ,  $D_A = (1 - \beta) \cdot \log_{10} e \simeq 0.434 \cdot (1 - \beta) \simeq 0.0347 - 0.0651$ , and the energy  $E$  is given in eV. Because of our lack of knowledge of the hadronic interactions at the highest energies, the value of  $a$  is highly model dependent and presents a large variability. It can be written as  $a = \log_{10}(N_\mu^p) - \beta \log_{10}(\zeta_c^\pi)$  and varies approximately from 6.5 to 8.0, depending on the hadronic interaction model. These values of  $a$  were obtained using the simulations described in Section 3.

In addition to the  $\langle \log_{10} N_\mu \rangle$ , the  $\sigma[\log_{10} N_\mu]$  could also be modeled by the same approach. However, no analytic model has been proposed to describe the shower-to-shower fluctuations and our study relies on simulations to propose a similar description of  $\sigma[\log_{10} N_\mu]$  evolution with energy and mass. We propose that the  $\sigma[\log_{10} N_\mu]$  can be described as

$$\sigma[\log_{10} N_\mu]_A = \sigma[\log_{10} N_\mu]_{\text{Fe}} + b \cdot [\ln(A) - \ln(56)]^2, \quad (4)$$

where  $\sigma[\log_{10} N_\mu]_{\text{Fe}}$  is the  $\sigma[\log_{10} N_\mu]$  for iron nucleus initiated showers. Two main assumptions were used in this proposal: a) for a fixed primary ( $A$ ), the  $\sigma[\log_{10} N_\mu]$  does not depend on energy and b) a quadratic dependency of  $\sigma[\log_{10} N_\mu]$  with  $\ln(A)$ . These assumptions are justified in Section 3 via Monte Carlo simulation of the air shower.

The description of the  $\sigma[\log_{10} N_\mu]$  is analogous to the deduction of  $\langle \log_{10} N_\mu \rangle$  using the Heitler–Matthews models in the following way. We will show in Section 3 that, for the purposes of this paper's analysis,  $\sigma[\log_{10} N_\mu]_{\text{Fe}}$  can be taken to be constant, in other words, the small model dependence of  $\sigma[\log_{10} N_\mu]_{\text{Fe}}$  can be ignored. On the other hand,  $b$  changes significantly with the hadronic interaction model, which reflects the theoretical uncertainties concerning the muonic component description.

Eqs. (3) and (4) summarize the first step of this paper. These equations offer a simple, but good description of the two first moments of the  $\log_{10} N_\mu$  distribution with energy and mass. The uncertainties due to hadronic interaction model descriptions are only significant for two parameters,  $a$  and  $b$ , while for the further parameters there is a good agreement between their predictions. The quality of the description given by Eqs. (3) and (4) is going to be numerically studied in the next section.

For a mixture of primaries in which each primary particle type,  $i$ , has mass  $A_i$  and contributes to the total flux with a fraction given by  $f_i$ , we can show that  $\langle \log_{10} N_\mu \rangle$  and  $\sigma[\log_{10} N_\mu]$  of the mixture ( $\text{mix}$ ) can be calculated as follows

$$\langle \log_{10} N_\mu \rangle_{\text{mix}} = \sum_i f_i \cdot \langle \log_{10} N_\mu \rangle_{A_i} \quad (5)$$

$$\langle \log_{10} N_\mu \rangle_{\text{mix}} = a + D_A \cdot \langle \ln(A) \rangle_{\text{mix}} + D_E \cdot (\log_{10} E - 19.0),$$

and

$$\sigma^2[\log_{10} N_\mu]_{\text{mix}} = \sum_i f_i \cdot \left[ \left( \langle \log_{10} N_\mu \rangle_{A_i} - \langle \log_{10} N_\mu \rangle_{\text{mix}} \right)^2 + \sigma^2[\log_{10} N_\mu]_{A_i} \right]. \quad (6)$$

Using Eq. (3) we can write

$$\sigma^2[\log_{10} N_\mu]_{\text{mix}} = \sum_i f_i \cdot \left[ D_A^2 \cdot (\ln(A_i) - \langle \ln(A) \rangle_{\text{mix}})^2 + \sigma^2[\log_{10} N_\mu]_{A_i} \right]. \quad (7)$$

Note that  $\sigma^2[\log_{10} N_\mu]_{\text{mix}}$  does not depend on  $a$ . The dependence on  $b$  is implicit in the  $\sigma^2[\log_{10} N_\mu]_{A_i}$  term.

### 3. Simulation studies of $\log_{10} N_\mu$ moments

In this section we briefly describe the procedure adopted to produce simulated  $\log_{10} N_\mu$  distributions that are extensively employed in the following sections of this paper. The present discussion is complemented by Appendix A where more details about the simulations are given. Furthermore, in this section we also use the simulated showers to validate the  $\log_{10} N_\mu$  moment descriptions proposed in Section 2 and to study the energy evolution of  $\log_{10} N_\mu$  moments for a set of mass composition scenarios.

#### 3.1. Simulation technique

In our analysis we aim to assess the number of muons measured in UHECR experiments. A combination of detector technology, observatory altitude, spatial configuration of the detectors and analysis procedures determines the lateral distance range and the energy threshold of detectable muons. To avoid saturation of the detectors (close to the shower axis) and large statistical fluctuations (far from the shower axis), a fiducial lateral distance range is commonly defined to get the lateral distance function integrated. Therefore, the measured number of muons ( $N_\mu^{\text{meas}}$ ) is not the total number of muons at the ground but only a sample of them above an energy threshold and within a distance range.

In this paper  $N_\mu^{\text{meas}}$  is defined as the number of muons with energy above 0.2 GeV reaching the ground (1400 m above sea level, the Auger mean altitude) at a distance between 500 m and 2000 m from the shower axis. This choice is motivated by the design of the main current high energy cosmic ray experiments, for example, the Pierre Auger Observatory [19] and Telescope Array [20].

The muons spatial and energy distributions at the ground can be evaluated by CORSIKA [21] (version 7.4000), which is a full Monte Carlo code able to perform 3D shower simulations.  $N_\mu^{\text{meas}}$  could be determined by CORSIKA, in despite of its high computational cost [22]. CONEX [23] (version 2r4.37) is a very fast hybrid simulation code which combines full Monte Carlo with solutions of one-dimensional cascade equations. From CONEX simulations it is possible to determine the total number of muons at the ground above 1 GeV ( $N_\mu^{\text{tot}}$ ).

$N_\mu^{\text{tot}}$  and  $N_\mu^{\text{meas}}$  can be simultaneously obtained from full simulated showers (CORSIKA), allowing us to parametrize the relation between them. We propose the following parametrization:

$$N_\mu^{\text{meas}} = R(E, X_{\text{max}}) \cdot N_\mu^{\text{tot}}, \quad (8)$$

where the conversion factor  $R$  should be determined for each primary and depends on the energy and  $X_{\text{max}}$ . The parametrization of  $R(E, X_{\text{max}})$  is explored in detail in Appendix A. The  $X_{\text{max}}$  dependence of the factor  $R$  ensures that the parametrization takes into account the shower-to-shower fluctuations due to the variance of the first interaction depth. Furthermore, the most relevant physical

processes responsible for muons production in showers are reliably reproduced by the CONEX simulations, and consequently they should also be represented in  $N_\mu^{\text{meas}}$ . As shown in Appendix A, the  $N_\mu^{\text{meas}}$  distributions obtained based on the proposed parametrization are in very good agreement with the ones obtained from full Monte Carlo simulation.

The parametrization was done only for shower at 38° zenith angle. The zenith angle dependence can be taken into account by simulating other primaries with the corresponding arrival direction and by dividing the data in zenith angle intervals.

#### 3.2. Simulating $\log_{10} N_\mu$ moments

We generated 60,000 CONEX (version 2r4.37) showers with energies between  $10^{18.4}$  and  $10^{19.6}$  eV, for four primaries (proton, helium, nitrogen and iron) and two hadronic interaction models (EPOS-LHC [24] and QGSJetII-04 [25]). The showers are distributed uniformly in  $\log_{10}(E)$  and the zenith angle is fixed at 38°. From the  $R(E, X_{\text{max}})$  parametrization of Appendix A, the CONEX showers were converted into a set of  $N_\mu^{\text{meas}}$ .

Fig. 1 shows the evolution of  $\langle \log_{10} N_\mu^{\text{meas}} \rangle$  with the primary mass for three energy intervals. Lines are the result of a linear fit which demonstrates the dependence of  $\langle \log_{10} N_\mu^{\text{meas}} \rangle$  with mass as proposed in Eq. (3). The fits resulted in  $D_A \simeq 0.034 - 0.037$  and  $a \simeq 6.64 - 7.70$ , with errors from the fit less than 0.0005 and 0.005, respectively.

The energy evolution of  $\langle \log_{10} N_\mu^{\text{meas}} \rangle$  is shown in Fig. 2, where one can note the linear behavior as proposed in Eq. (3). The fits resulted in  $D_E \simeq 0.915 - 0.928$ , with errors from the fit less than 0.0003. The energy evolution of  $\sigma[\log_{10} N_\mu^{\text{meas}}]$  is shown in Fig. 3. Note the flatness of  $\sigma[\log_{10} N_\mu^{\text{meas}}]$  and the coincidence of the  $\sigma[\log_{10} N_\mu^{\text{meas}}]$  constant value of iron initiated showers for both hadronic interaction models. These figures validate both assumptions made in Section 2 concerning  $\sigma[\log_{10} N_\mu^{\text{meas}}]$ .

The primary mass dependence of  $\sigma[\log_{10} N_\mu^{\text{meas}}]$  can be seen in Fig. 4 for three energy intervals and both hadronic interaction models. The dashed lines are the quadratic curves shown in Eq. (4) fitted to the points. The fits resulted in  $\sigma[\log_{10} N_\mu]_{\text{Fe}}$  being indeed nearly constant, varying from 0.0258 to 0.0275, with errors from the fits less than 0.003. The fit also resulted in  $b = 0.0024 \pm 0.0002$  for QGSJetII-04 and  $b = 0.0033 \pm 0.0003$  for EPOS-LHC. The simulations shown in this section confirmed all the assumptions made in Section 2.

### 4. Mass composition scenarios and the energy evolution of the $\log_{10} N_\mu$ moments

In this section we simulate the energy evolution of  $\log_{10} N_\mu^{\text{meas}}$  moments for six mass composition scenarios, which are defined by setting the fractions  $f_i(E)$  of the total flux corresponding to each particle with mass  $A_i$ . Given  $f_i(E)$  and  $A_i$  we can calculate  $\langle \log_{10} N_\mu^{\text{meas}} \rangle$  and  $\sigma[\log_{10} N_\mu^{\text{meas}}]$  as a function of energy using the procedure described in Sections 2 and 3.

The mass composition scenarios we used are divided in two groups. The first one includes the astrophysical motivated scenarios, which are labeled by the letter A. The second group includes two scenarios obtained from the  $X_{\text{max}}$  distributions fit performed by the Pierre Auger Collaboration [11,16] and they are labeled by the letter X. Below, we present a brief description of the composition scenarios, which can be skipped by the reader that is familiar with the subject.

**Scenario A1:** This scenario proposes a pure proton flux. It was the first model proposed to explain the dip in the energy spectrum as the effect of pair-production in the propagation of the UHECR. This model is described in Refs. [5,8] and was also explored in Refs. [6,15] (labeled as Model B in Ref. [15]).

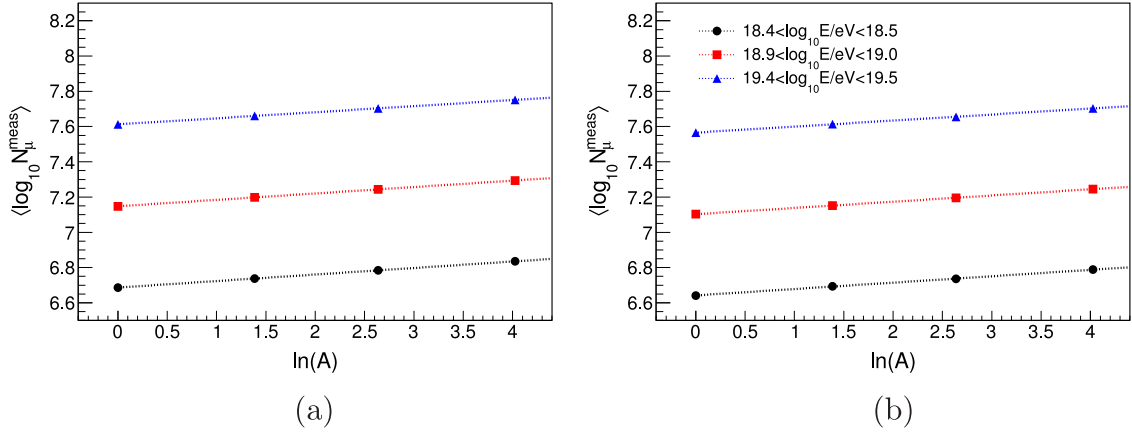


**Fig. 1.**  $\langle \log_{10} N_{\mu}^{\text{meas}} \rangle$  as a function of  $\ln(A)$  for both hadronic interaction models, (a) EPOS-LHC and (b) QGSJetII-04 and three energy intervals. The dotted lines are the results of the linear fit, represented in Eq. (3). The statistical error bars are smaller than the markers.

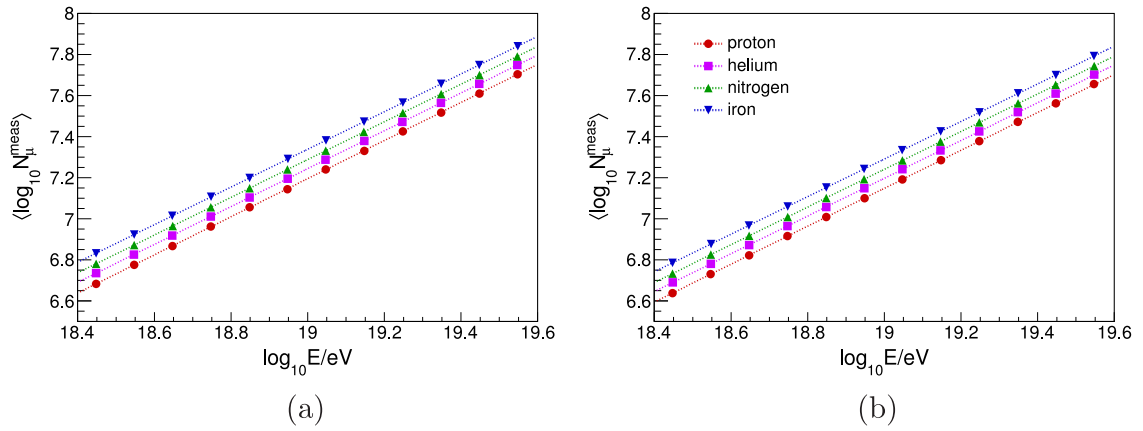


**Fig. 2.**  $\langle \log_{10} N_{\mu}^{\text{meas}} \rangle$  as a function of  $\log_{10}(E)$  for both hadronic interaction models, (a) EPOS-LHC and (b) QGSJetII-04, and four primaries (proton, helium, nitrogen and iron). The dotted lines are the results of the linear fit, represented in Eq. (3). The statistical error bars are smaller than the markers.

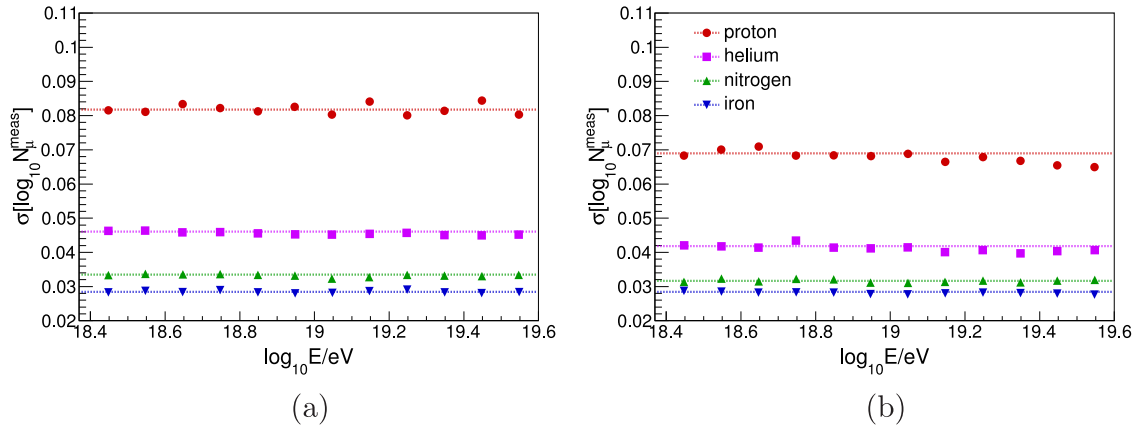


**Fig. 3.**  $\sigma[\log_{10} N_{\mu}^{\text{meas}}]$  as a function of  $\log_{10}(E)$  for both hadronic interaction models, (a) EPOS-LHC and (b) QGSJetII-04, and four primaries (proton, helium, nitrogen and iron). The dotted lines are the results of the fit of a constant energy function. The statistical error bars are smaller than the markers.

**Scenario A2:** This scenario assumes a mixed source composition with abundances similar to the data at lower energies. It was proposed by Allard et al. (labeled as Model A in Ref. [15]). In this model the ankle is explained as the transition in the predominance of the flux from the galactic to the extra-galactic component. The abundances are originally given for five groups of nuclei, however, in this paper the fluxes of the two heaviest groups were summed into the iron component.

**Scenario A3:** Biermann and de Souza [9] have proposed a model in which the observed cosmic ray energy spectrum from  $10^{15.0}$  to  $3 \times 10^{20.0}$  eV is explained by the galactic and only one extra-galactic source, the radio galaxy Cen A. In this model the element abundances from extra-galactic origin are similar to the galactic ones, but shifted up in energy because of the relativistic shock in the jet emanating from the active black hole. The abundances are originally given for six groups of nuclei, however, in this paper the flux of

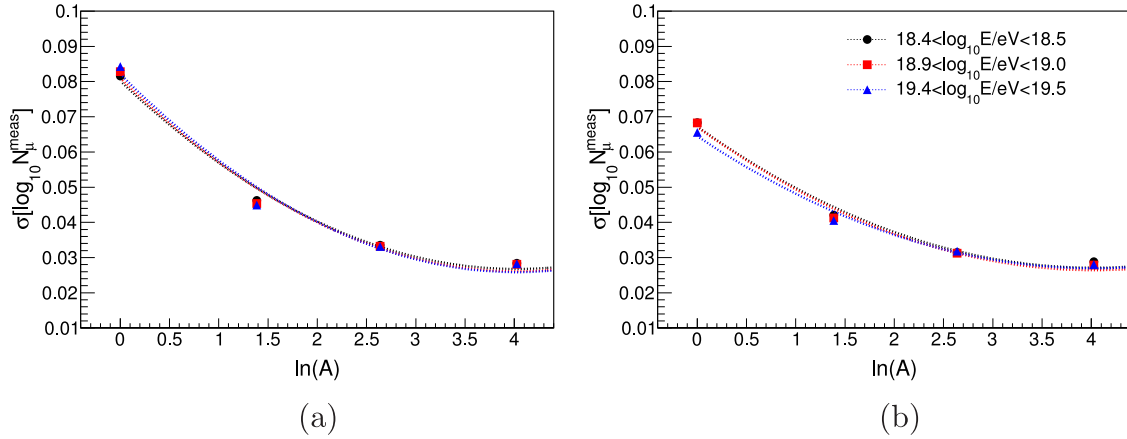


**Fig. 4.**  $\sigma[\log_{10} N_{\mu}^{\text{meas}}]$  as a function of  $\ln(A)$  for both hadronic interaction models, (a) EPOS-LHC and (b) QGSJetII-04, and three energy intervals. The dotted lines are the results of the fit of Eq. (4). The statistical error bars are smaller than the markers.

the element group Ne–S was summed into the nitrogen flux and the flux of the Cl–Mn group was summed into the iron group flux.

**Scenario A4:** The model proposed by Globus et al. [7] describes the whole cosmic ray spectrum by superposing a rigidity dependent galactic component and a generic extra-galactic component. This model gives an adequate description of the energy spectrum and the moments of the  $X_{\text{max}}$  distribution measured by the Pierre Auger Observatory.

**Scenario X1:** It has been shown by the Pierre Auger Collaboration that the measured  $X_{\text{max}}$  distributions can be well described by a combination of four components [11,16]. By fitting the  $X_{\text{max}}$  simulated distributions to the data, the abundances of the separate components were obtained as a function of energy. This scenario is based on the abundances obtained by using the hadronic interaction model QGSJetII-04. However, the abundances obtained with Sibyll2.1 are also very close to the one we used. In order to minimize point-to-point fluctuations, we used here a smooth curve fitted to the fractions obtained in the Auger analysis [16].

**Scenario X2:** This scenario was obtained by fitting  $X_{\text{max}}$  distributions measured by the Pierre Auger Observatory using showers simulated with the EPOS-LHC hadronic interaction model. The procedure is the same as the one adopted for Scenario X1.

The merging of components done for models A2 and A3 is necessary to allow us to use the parametrization elaborated in Section 3. Since we present in this paper only the analysis procedure, verified with simulations, this choice has no limiting consequence. Besides that, the systematic uncertainties of the abundances obtained from the scenarios are also going to be neglected here. Figs. 5 and 6 show the abundances for each scenario in the energy range from  $10^{18.4}$  to  $10^{19.6}$  eV as explained above. Scenario A1 is not shown because it assumes a 100% proton flux.

Fig. 7 shows the energy evolution of the  $\langle \log_{10} N_{\mu}^{\text{meas}} \rangle$  and  $\sigma[\log_{10} N_{\mu}^{\text{meas}}]$  for all mass composition scenarios. The error bars correspond to the one sigma fluctuation of the mean value considering the statistics from 3 years of AugerPrime data (3000 km<sup>2</sup> of muon detectors). The all particle flux was taken from Ref. [3]. Fig. 7a shows the mean normalized to the proton simulation for better visualization.

## 5. Discrimination between mass composition scenarios

Given the theoretical uncertainties on the  $N_{\mu}$  predictions and the systematic uncertainties on the energy reconstruction, the

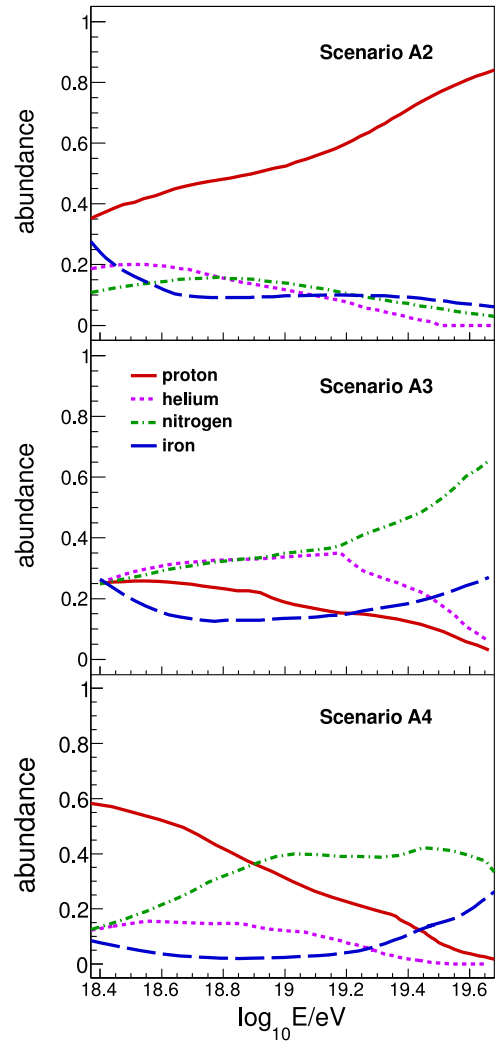


**Fig. 5.** The composition component abundances as a function of  $\log_{10}(E)$  for the mass composition scenarios A2, A3 and A4 (see text).

question we would like to answer in this section is how it is possible to discriminate between the mass composition scenarios shown above using the evolution of the  $\log_{10} N_{\mu}^{\text{meas}}$  moments with energy. Examining Fig. 7 it might seem easy to differentiate

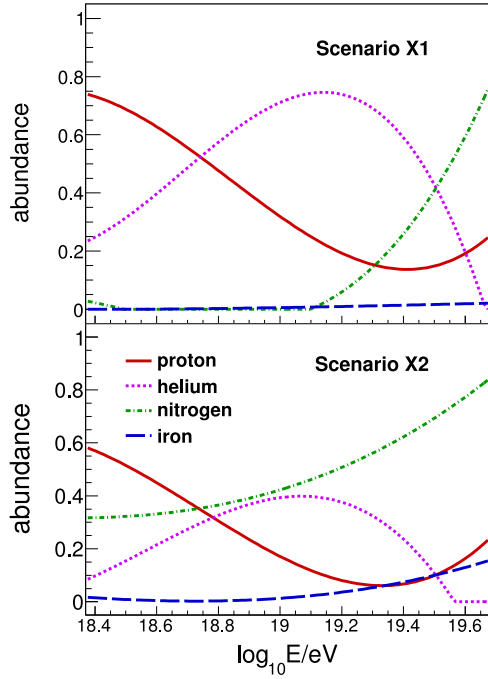


**Fig. 6.** The composition component abundances as a function of  $\log_{10}(E)$  for the mass composition scenarios X1 and X2 (see text).

the scenarios by using the absolute value or the evolution of the  $\log_{10} N_{\mu}^{\text{meas}}$  moments with energy. However, if we include in this figure the uncertainties in the hadronic interaction model and systematic in energy reconstruction the interpretation of the data is not straightforward.

Fig. 8 shows how the uncertainties on the hadronic interaction model predictions and on the energy reconstruction influence the interpretation of the  $\langle \log_{10} N_{\mu}^{\text{meas}} \rangle$  in terms of composition. We show in this figure the extreme composition scenarios (A1 and A3), since the other four scenarios lie within them. In Fig. 8a we calculate  $\langle \log_{10} N_{\mu}^{\text{meas}} \rangle$  for scenarios A1 and A3 adding arbitrarily 20% more muons to the simulation predictions to mimic the theoretical uncertainties in the hadronic interaction model predictions [14]. Even the extreme models A1 and A3 would overlap if the uncertainty is considered. In Fig. 8b we calculate  $\langle \log_{10} N_{\mu}^{\text{meas}} \rangle$  for scenarios A1 and A3 and changed the simulated energy by  $\pm 15\%$  in order to evaluate the effect of the systematic uncertainty in the energy reconstruction. Once more it is clear that even the extreme

scenario cases cannot be distinguished anymore. Moreover a combination of both uncertainties in the  $N_{\mu}$  predictions and energy applied to this analysis would make the discrimination between the scenarios even harder. The conclusion is clear: the measurement of  $N_{\mu}$  does not lead to a straightforward interpretation of the data in terms of composition if all the uncertainties are considered.

It is worthwhile to remember here how the interpretation of the  $X_{\text{max}}$  measurement is done. The Pierre Auger Collaboration, for example, fits  $f_i$  to the measured  $X_{\text{max}}$  distribution in bins of energy [16]. The calculation of  $f_i$  depends on simulation and therefore on the hadronic interaction model. However, because the electromagnetic cascade of the shower dominates the determination of the  $X_{\text{max}}$  position, the discrepancy between the hadronic interaction model  $X_{\text{max}}$  predictions is minimized. The difference in  $\langle X_{\text{max}} \rangle$  is at most 20 g/cm<sup>2</sup> and in  $\sigma[X_{\text{max}}]$  is 6 g/cm<sup>2</sup> for the most often used hadronic interaction models (EPOS-LHC, Sibyll2.1 and QGSJetII-04) [11]. Given the small differences in the predictions of  $X_{\text{max}}$  and its consistency with data, the fit of  $f_i$  leads to acceptable differences in the calculation of  $f_i$  for different hadronic interaction models and then to mass composition scenarios which are physically consistent.

Unfortunately, the same procedure cannot be applied to  $N_{\mu}$  because of the discrepancies between the hadronic interaction model predictions and the inconsistency between simulations and data. It is known that the simulations are off by at least 20% in the calculation of  $N_{\mu}$  [13,14]. A fit of  $f_i$  based on the  $N_{\mu}$  distribution would lead to non-physical results. Therefore we propose an alternative analysis to discriminate between composition scenarios. The idea is to fix  $f_i$ , choosing a mass composition scenario, and fit the data with the energy evolution of  $\log_{10} N_{\mu}^{\text{meas}}$  moments to search for the scenarios which better describe the data.

If the composition ( $f_i$ ) were known by an independent measurement, this procedure would allow us to calculate  $a$  and  $b$  and constrain the hadronic interaction models by limiting fundamental properties of the interactions. This hypothesis needs to be explored further by using the results from the  $X_{\text{max}}$  measurement to fix  $f_i$ .

We propose here a procedure that allows a statistically robust test of composition scenarios against data. The method starts by using the model proposed in Section 2 to predict the energy evolution of  $\langle \log_{10} N_{\mu}^{\text{meas}} \rangle$  and  $\sigma[\log_{10} N_{\mu}^{\text{meas}}]$  for a given composition scenario. Here, all the parameters of the model are fixed, except  $a$  and  $b$ . The next step is to compare these predictions with data and find the values of  $a$  and  $b$  which make the model most similar to the data. This can be done by a  $\chi^2$  minimization. The minimal values of  $\chi^2$  determine which scenario best describes the data. Since  $a$  and  $b$  take all the hadronic interaction model dependence, the

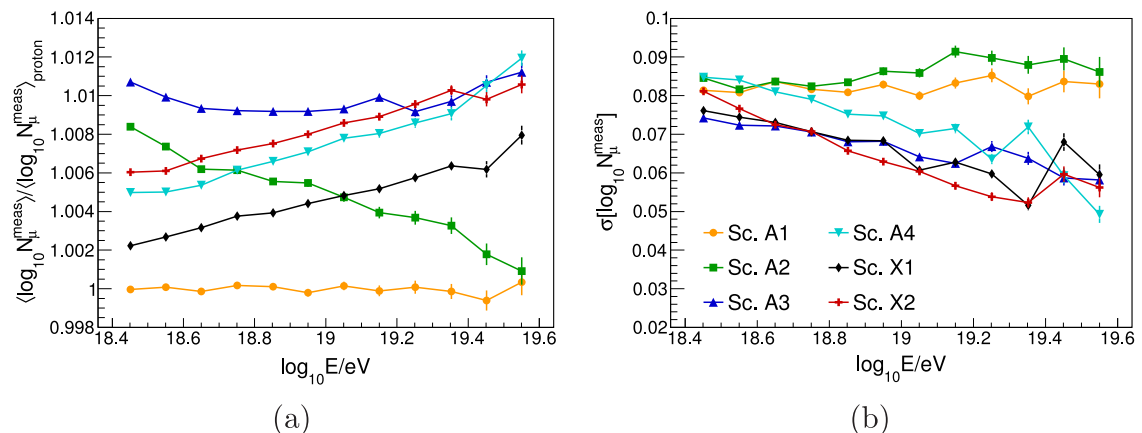


**Fig. 7.** Energy evolution of (a)  $\langle \log_{10} N_{\mu}^{\text{meas}} \rangle$  and (b)  $\sigma[\log_{10} N_{\mu}^{\text{meas}}]$  for the six composition scenarios described in the text. The values of  $\langle \log_{10} N_{\mu}^{\text{meas}} \rangle$  are divided by the corresponding value of pure proton composition for better visualization. The hadronic interaction model used was EPOS-LHC.

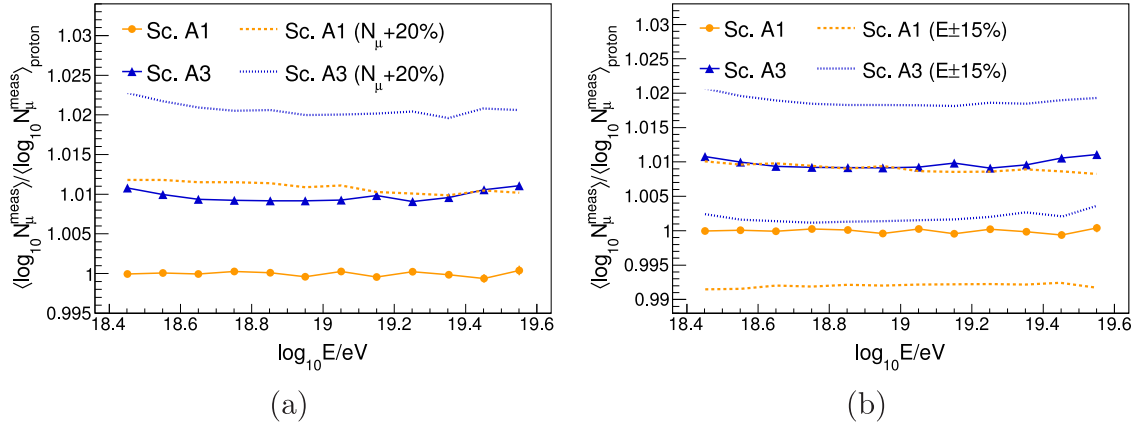


**Fig. 8.** Energy evolution of  $\langle \log_{10} N_{\mu}^{\text{meas}} \rangle$  for 2 mass composition scenarios, A1 and A3. The dashed lines show the effects of (a) an increase of 20% in the  $N_{\mu}$  and (b) a variation of  $\pm 15\%$  in energy. The values of  $\langle \log_{10} N_{\mu}^{\text{meas}} \rangle$  are divided by the corresponding value of pure proton composition for better visualization. The hadronic interaction model used was EPOS-LHC.

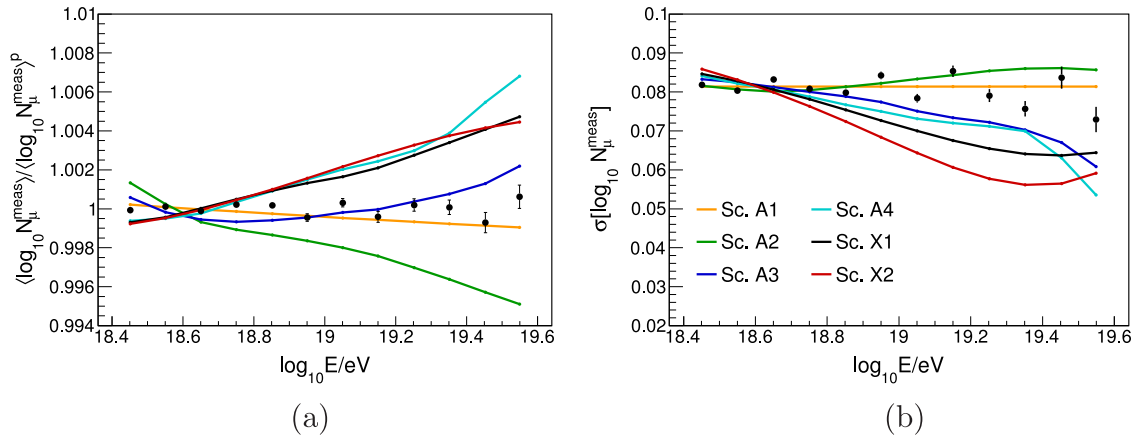


**Fig. 9.** Black dots show the simulated (a)  $\langle \log_{10} N_{\mu}^{\text{meas}} \rangle$  and (b)  $\sigma[\log_{10} N_{\mu}^{\text{meas}}]$  using scenario A1 as the true one. The colored lines show the results of the fit for each one of the test scenarios. The values of  $\langle \log_{10} N_{\mu}^{\text{meas}} \rangle$  are divided by the corresponding value of pure proton composition for better visualization.

composition scenario can be tested independently of hadronic interaction model limitations.

We explored this analysis proposal by choosing a composition scenario as if it would represent the true measurement, and we name it *true scenario*. We generate the  $\log_{10} N_{\mu}$  moments as a function of energy for the *true scenario* using the simulation described in Section 3 in order to emulate the real data. Here, the energy bins are defined by 12 intervals of width  $\Delta \log_{10}(E/\text{eV}) = 0.1$ , from  $10^{18.4}$  to  $10^{19.6}$  eV. This choice is mainly motivated by the Auger experimental acceptance, which reaches a 100% efficient trigger probability around  $10^{18.4}$  eV [26]. The number of events in each bin is determined by considering 3 years of data taken by the full array of Auger, following the energy spectrum of Ref.[3].

It is important to note that the simulations used here do not take into account any detector effects or zenith angle dependence. Although in this paper we do not intend to approach these issues because the focus here are on the general aspects of the analysis, it is clear that in practical applications of the method one should deal with these experimental difficulties. The detector effects, like resolution and limited acceptance, could be addressed by unfolding or unbiasing techniques once the detector response is well known. One example of these process is the Auger analysis of  $X_{\text{max}}$  moments [11]. The zenith angle dependence could be addressed in a conservative approach by dividing the data in zenith angle intervals or by correcting the data using a *constant intensity cut* (CIC) method [27–29]. This later class of method has been successfully used, for example, to determine the shower size

parameter by Pierre Auger [30] and KASCADE-Grande Collaboration [31] and to correct the  $N_{\mu}$  parameter by KASCADE-Grande Collaboration [32]. The systematics uncertainties from these procedure are usually small ( $< 10\%$ ) and should be taken into account in a realistic approach of our method.

In next step, we perform a  $\chi^2$  fit using the model described by Eqs. (5) and (7), with  $a$  and  $b$  as free parameters of the fit, for all the composition scenarios. The scenarios which are not the true one are named *test scenarios*. Fig. 9 shows one realization of these fits in which scenario A1 was used as the *true scenario* to generate the black dots. The fit of the  $\langle \log_{10} N_{\mu}^{\text{meas}} \rangle$  with energy (Fig. 9) sets the best value of  $a$  and the minimal value of  $\chi^2(a)$ . The fit of the  $\sigma[\log_{10} N_{\mu}^{\text{meas}}]$  with energy (Fig. 9) sets the best value of  $b$  and the minimal value of  $\chi^2(b)$ . In all fits,  $D_E = 0.920$ ,  $D_A = 0.0354$  and  $\sigma[\log_{10} N_{\mu}]_{\text{Fe}} = 0.0265$ . Each line in Fig. 9 is the fit of one out of the six composition scenarios. We compared all scenarios (*test scenarios*) to the *true scenario*.

A simple  $\chi^2$  comparison finds the *test scenarios* which best fit the data generated with the *true scenario*. The average value of  $\chi^2$  as a function of the fitted parameters  $a$  and  $b$  is shown in Fig. 10 for a set of 500 realizations. In this case, it is clear that the scenario A1 better describes the  $\langle \log_{10} N_{\mu}^{\text{meas}} \rangle$  and  $\sigma[\log_{10} N_{\mu}^{\text{meas}}]$  evolution with energy because of the smaller values of  $\chi_{\text{min}}^2(a)$  and  $\chi_{\text{min}}^2(b)$ . Fig. 11 shows the plots of  $\chi_{\text{min}}^2(a)$  vs  $\chi_{\text{min}}^2(b)$  for all six scenarios as the *true scenarios*. The error bars represent one standard deviation around the mean for 500 realizations. All scenarios,

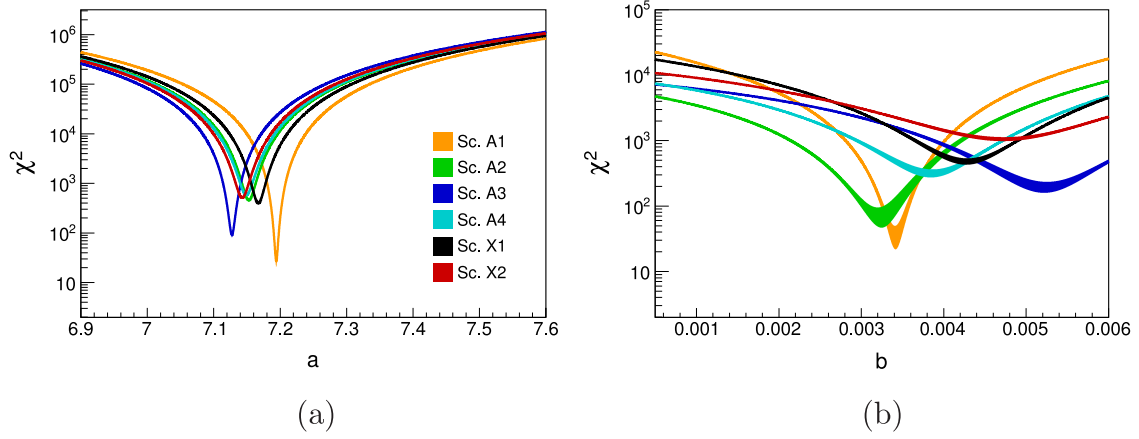


Fig. 10.  $\chi^2$  as a function of the parameters  $a$  (a) and  $b$  (b) for all the scenarios. The scenario A1 is the *true scenario*. The colored bands represent one standard deviation around the mean for a set of 500 realizations.

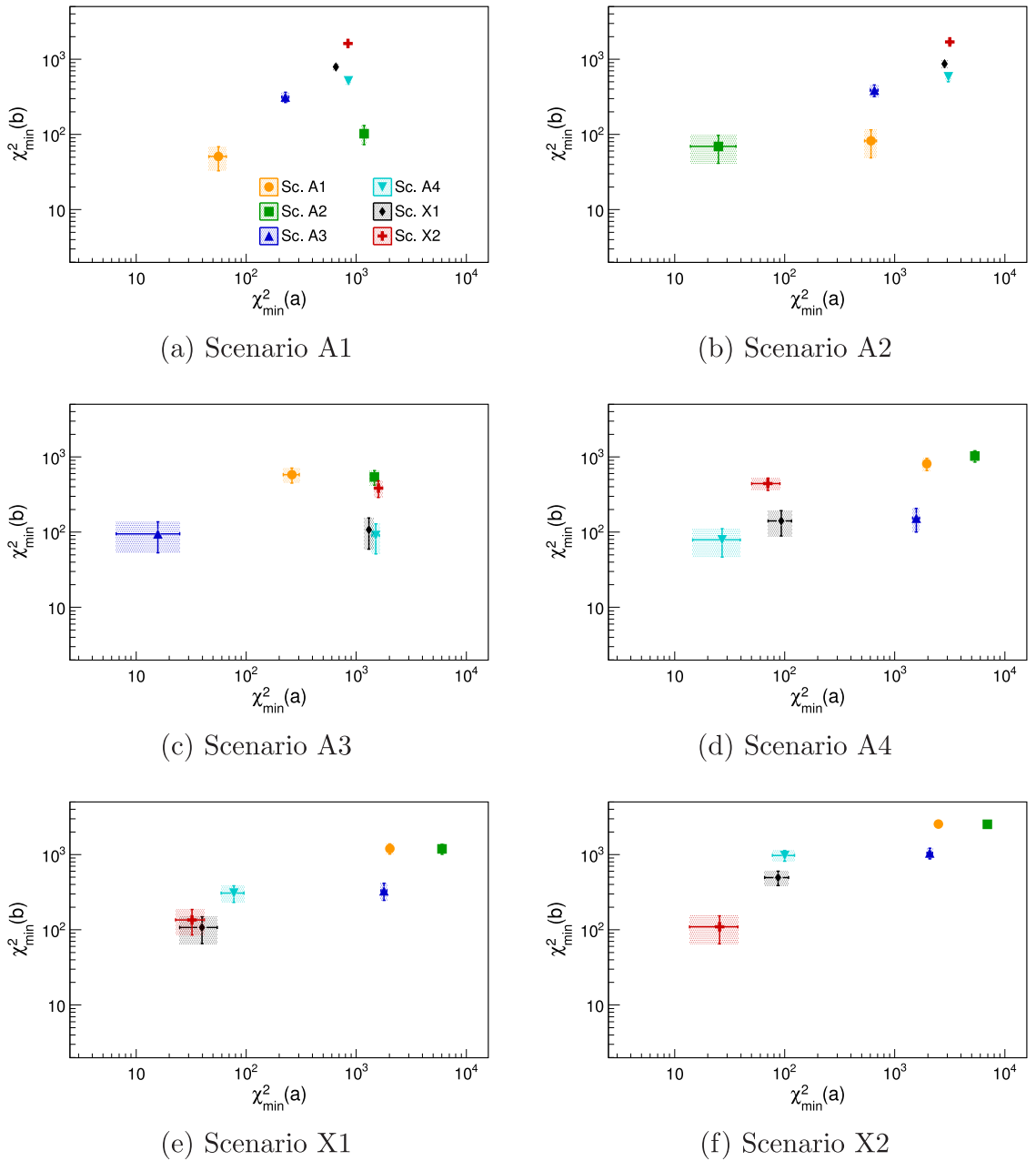
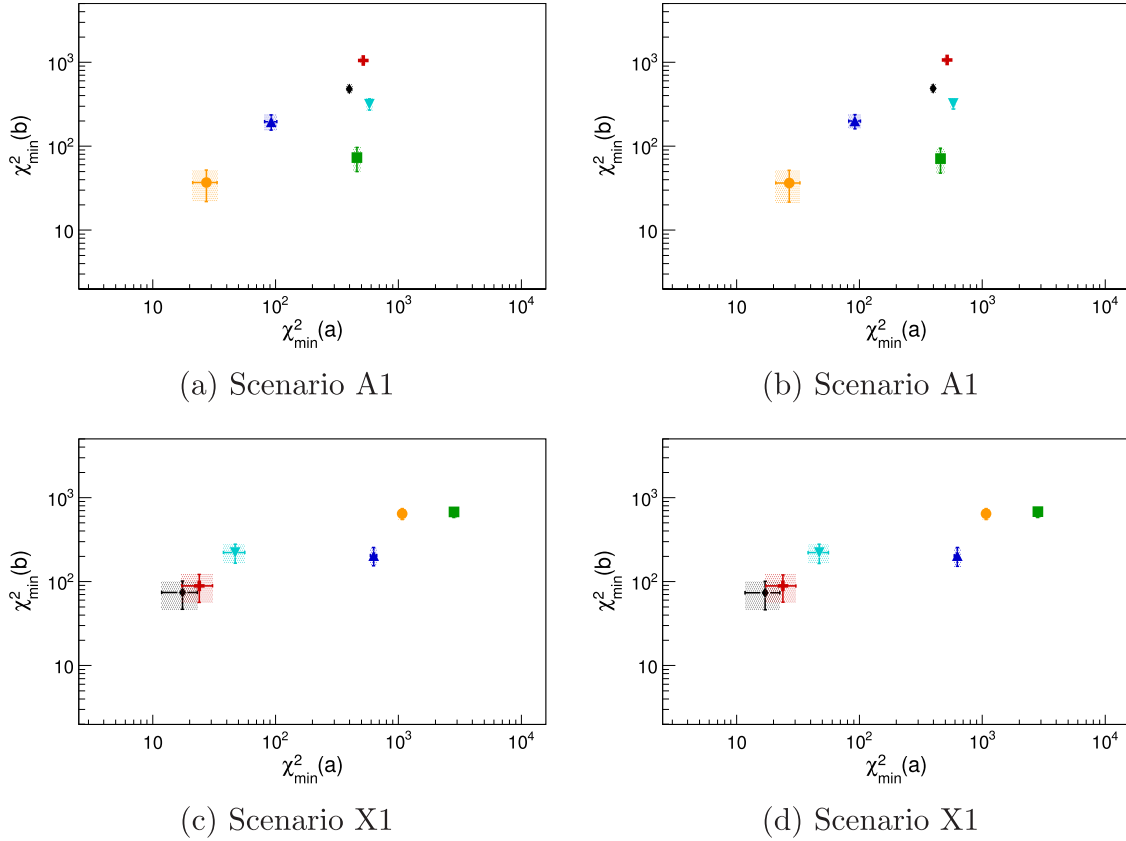


Fig. 11.  $\chi_{\min}^2(a)$  vs  $\chi_{\min}^2(b)$  for all composition scenarios.



**Fig. 12.**  $\chi^2_{\min}(a)$  vs  $\chi^2_{\min}(b)$  for the true scenario A1 with (a)  $\alpha_{N_\mu} = 1.3$  and (b)  $\alpha_{N_\mu} = 1.6$  and for the true scenario X1 with (c)  $\alpha_{N_\mu} = 1.3$  and (d)  $\alpha_{N_\mu} = 1.6$  (see text).

except in X1 case, can be discriminated by the smallest  $\chi^2_{\min}(a)$  and  $\chi^2_{\min}(b)$ . In other words, the *true scenario* is the one with the  $\chi^2_{\min}(a) - \chi^2_{\min}(b)$  point closer to the left-down corner. Note that only  $\chi^2_{\min}(a)$  or only  $\chi^2_{\min}(b)$  cannot alone discriminate most of the scenarios. In the case of X1 as *true scenario* one can see that, even if it is not possible to discriminate scenario X1 and X2, it is still possible to discriminate the  $X_{\max}$  scenarios from the astrophysical ones.

### 5.1. Sensitivity to the systematic uncertainties on energy scale and absolute number of muons

As mentioned above, the greatest obstacles in interpreting  $N_\mu$  data currently are the systematic uncertainties in the theoretical description and reconstruction of air showers. In this section we demonstrate that the procedure proposed in the previous section to discriminate between composition scenarios is stable under systematic changes of absolute  $N_\mu$  prediction and of energy scale.

The systematic uncertainties in  $N_\mu$  scale were tested by applying the rescaling factor  $\alpha_{N_\mu}$  in  $N_\mu^{\text{meas}}$  generated by simulations. The examination of Eq. (3) shows that a rescaling factor on  $N_\mu$  corresponds to an additive term in  $a$ . This is how the systematic effect on  $N_\mu^{\text{meas}}$  is incorporated in the simple description of  $\langle \log_{10} N_\mu^{\text{meas}} \rangle$ . Eq. (4) shows that  $b$  does not depend on  $\alpha_{N_\mu}$ . If only  $\langle \log_{10} N_\mu^{\text{meas}} \rangle$  changes by an additive term when  $\alpha_{N_\mu}$  is applied, it is clear that  $\chi^2_{\min}(a)$  and  $\chi^2_{\min}(b)$  are independent of  $\alpha_{N_\mu}$ . Fig. 12 shows the values of  $\chi^2_{\min}(a)$  and  $\chi^2_{\min}(b)$  for true scenarios A1 and X1 and  $\alpha_{N_\mu} = 1.3$  and 1.6, as examples. One can see that the values of  $\chi^2_{\min}(a)$  and  $\chi^2_{\min}(b)$  are stable under systematic changes in  $N_\mu^{\text{meas}}$ .

The energy scale effect was tested by including a rescaling factor  $\alpha_E$  in simulated energy of each shower. The same analysis of Eqs. (3) and (4) reveals that  $a$  and  $b$  accommodate the sys-

tematic effects in energy as additive terms. All additive terms are canceled in the  $\chi^2$  comparison resulting in the independence of the conclusions under systematic effects. In Fig. 13 we show the  $\chi^2_{\min}(a)$  and  $\chi^2_{\min}(b)$  for true scenarios A1 and X1 and for  $\alpha_E = 0.85$  and 1.15, which represents a systematic uncertainties of 15% in energy. Again, it can be observed that the values of  $\chi^2_{\min}(a)$  and  $\chi^2_{\min}(b)$  would not lead to a different conclusion, and therefore, the results of the method would be stable under energy shifts.

## 6. Conclusion

In this paper, we have analyzed the muon content of air showers, proposed a parametrization of the first two moments of the number of muons with energy and primary particle mass and showed how the measured mean and  $\sigma$  of  $\log_{10} N_\mu$  can be used to discriminate between composition scenarios.

We proposed a model to describe  $\langle \log_{10} N_\mu^{\text{meas}} \rangle$  and  $\sigma[\log_{10} N_\mu^{\text{meas}}]$  as a function of energy and primary particle mass ( $A$ ). This model was conceived to keep the most relevant hadronic interaction uncertainties concentrated in only two parameters ( $a$  and  $b$ ). We have validated the model with Monte Carlo simulation of the air shower and its capability to describe the  $\log_{10} N_\mu^{\text{meas}}$  moments was proven.

Six composition scenarios were considered. The particle flux predicted by these scenarios was transformed into the corresponding  $\langle \log_{10} N_\mu^{\text{meas}} \rangle$  and  $\sigma[\log_{10} N_\mu^{\text{meas}}]$  evolution with energy. The  $\langle \log_{10} N_\mu^{\text{meas}} \rangle$  and  $\sigma[\log_{10} N_\mu^{\text{meas}}]$  evolution with energy was fitted using the proposed parametrization. A comparison of the  $\langle \log_{10} N_\mu^{\text{meas}} \rangle$  and  $\sigma[\log_{10} N_\mu^{\text{meas}}]$  model using a simple  $\chi^2$  test allows the discrimination between the scenarios. The discrimination is effective even considering the systematic uncertainties on the  $N_\mu$  prediction and on energy scale uncertainty.

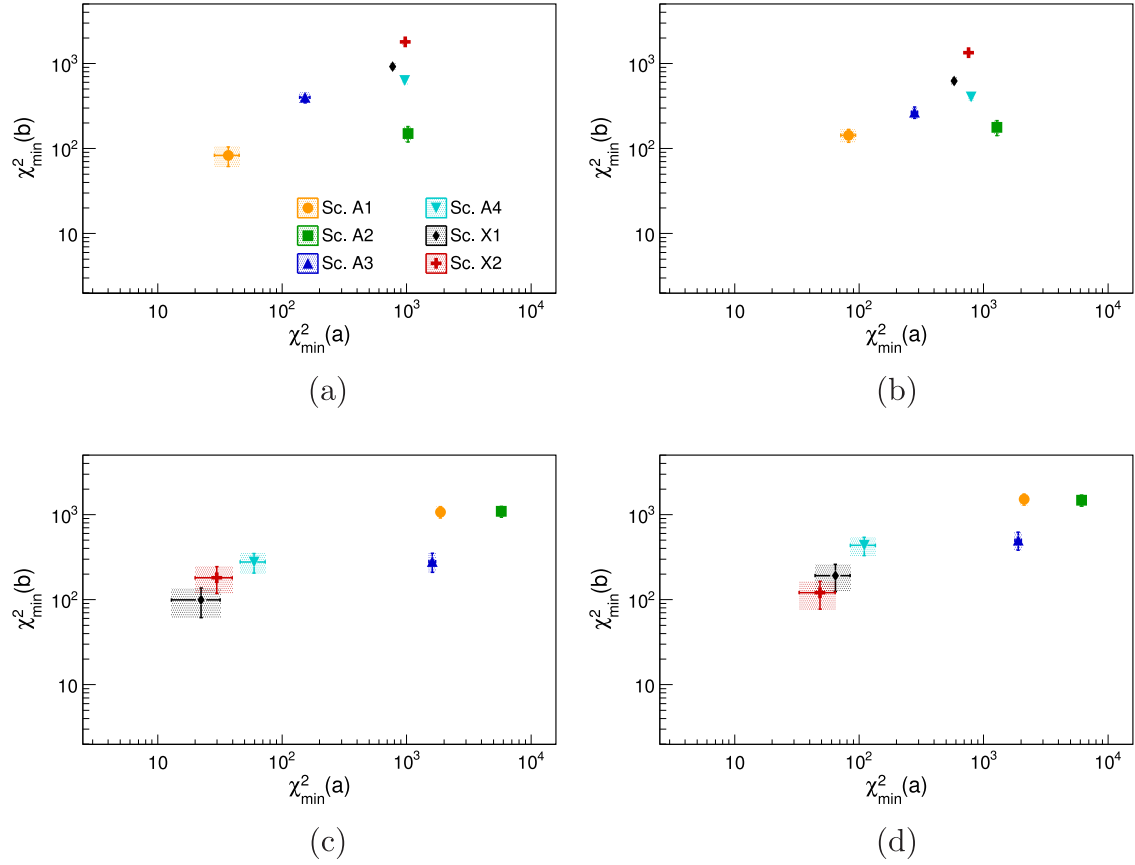


**Fig. 13.**  $\chi^2_{\min}(a)$  vs  $\chi^2_{\min}(b)$  for the true scenario A1 with (a)  $\alpha_E = 0.85$  and (b)  $\alpha_E = 1.15$  and for the true scenario X1 with (c)  $\alpha_E = 0.85$  and (d)  $\alpha_E = 1.15$  (see text).

The effect of the systematic in the  $N_\mu$  number and energy reconstruction was studied for constant values of the uncertainty with energy. This choice is justified by the narrow energy interval used in the analysis. Abrupt changes of the systematic uncertainties with energy could change the conclusion drawn here since  $\log_{10} N_\mu^{\text{meas}}$  is assumed to be fixed in the proposed model.

The upgrade of Telescope Array [33] and Pierre Auger Observatory [34], to be constructed in the next few years, will for the first time allow precise measurements of the muon component of air showers for energies above  $10^{18}$  eV. This will open up a new window of analyses and tests in astroparticle physics. Once data is acquired, the parametrization proposed here could be tested and if proven to be right, the analysis method proposed in Section 5 could be used to find the most probable composition scenario in the energy range from  $10^{18.4}$  to  $10^{19.6}$  eV.

### Acknowledgments

We thank Stéphane Coutu and Carola Dobrigkeit for the review of the manuscript on behalf of the Pierre Auger Collaboration. RRP thanks the financial support given by FAPESP (2014/10460-1). RC and MP gratefully acknowledge the financial support by Fundação para a Ciência e Tecnologia (SFRH/BPD/73270/2010) and OE, FCT-Portugal, CERN/FIS-NUC/0038/2015. VdS thanks the support of the Brazilian population via CNPq and FAPESP (2010/07359-6, 2014/19946-4).

### Appendix A. Parametrization of $R(E, X_{\max})$

As mentioned in Section 3, the parametrization of  $R(E, X_{\max})$  can be done by means of full air shower simulations. In this paper, we choose CORSIKA [21] as the full Monte Carlo code.

First, a set of 200 CORSIKA (version 7.4000) showers for each primary (proton, helium, nitrogen and iron), fixed energy ( $E = 10^{18.5}, 10^{19.0}, 10^{19.5}$  eV) and high energy hadronic interaction model (EPOS-LHC [24] and QGSJetII-04 [25]) were generated. The low energy hadronic interaction model is Fluka [35] in all cases. Furthermore, the zenith angle was set fixed to  $38^\circ$  for all showers. This is clearly a simplification, and then it should be stressed that, in a more realistic analysis, the  $N_\mu$  zenith angle dependence must be treated.

In Fig. A.1 the factor  $R$  is shown as a function of  $X_{\max}$  for all primaries, one primary energy,  $10^{19.0}$  eV, and one hadronic interaction model, EPOS-LHC. The observed behavior suggests a linear parametrization of the form,

$$R(E, X_{\max}) = p_1(E) \cdot X_{\max} + p_0(E), \quad (\text{A.1})$$

where  $p_0$  and  $p_1$  have to be also parametrized as a function of energy. The values of  $p_0$  and  $p_1$  for each primary and energy were determined from the linear fit, shown in Fig. A.1 by a dotted red line.

In Fig. A.2  $p_0$  and  $p_1$  are shown as a function of logarithmic energy for all primaries and the hadronic interaction model EPOS-LHC, as an example. Again, we are able to perform a linear parametrization of  $p_0$  and  $p_1$  as a function of  $\log_{10}(E)$ , in the form

$$\begin{aligned} p_0(E) &= \alpha_0 \cdot \log_{10}(E/\text{eV}) + \beta_0, \\ p_1(E) &= \alpha_1 \cdot \log_{10}(E/\text{eV}) + \beta_1. \end{aligned} \quad (\text{A.2})$$

The dotted lines in Fig. A.2 show the function from Eq. (A.2) fitted to the point obtained from CORSIKA simulations. The values of  $\alpha_0$ ,  $\beta_0$ ,  $\alpha_1$  and  $\beta_1$  for all primaries and hadronic interaction models are presented in Table A.1.

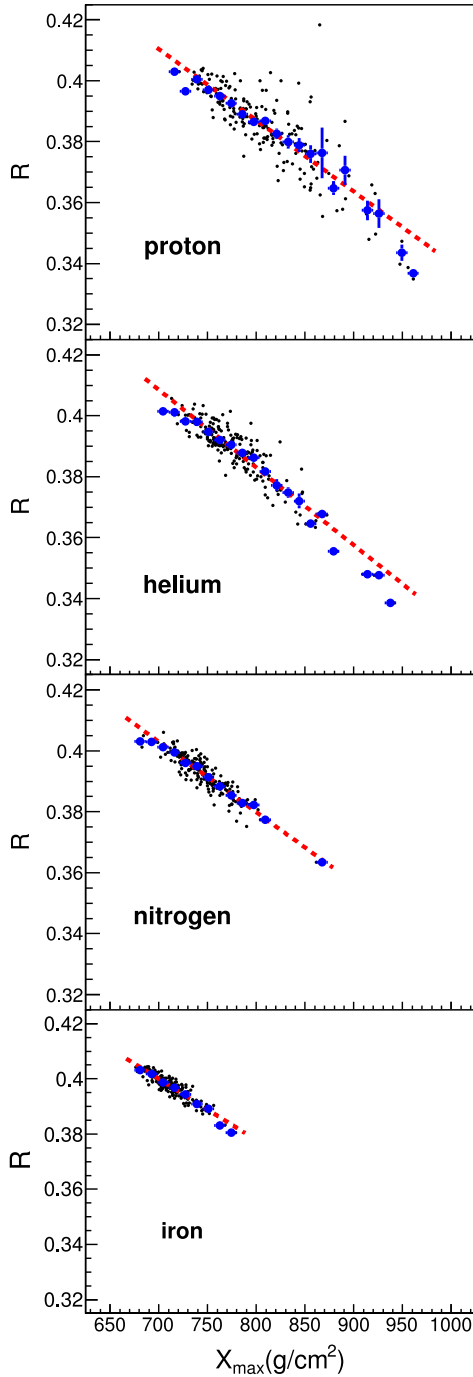


**Fig. A.1.** Conversion factor  $R$  as a function of  $X_{\max}$  for  $E = 10^{19.0}$  eV showers with EPOS-LHC as hadronic interaction model. The black dots are individual showers, the blue circles are the profile and dotted red line is the linearfit. (For interpretation of the references to color in this figure legend, the reader is referred to the web version of this article.)

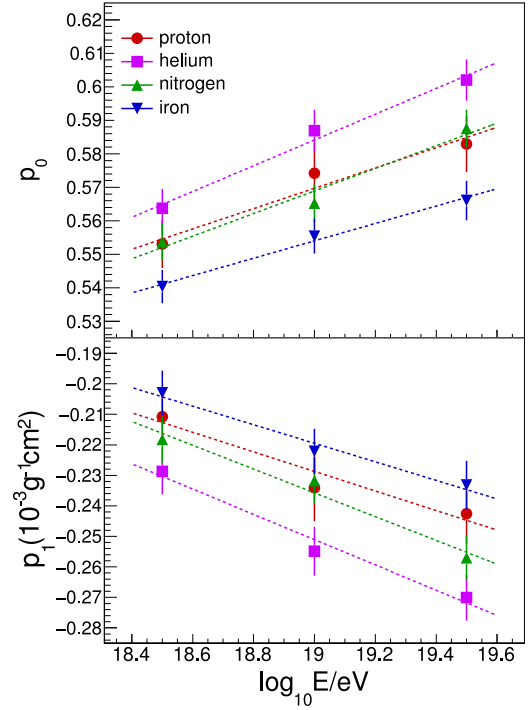


**Fig. A.2.**  $p_0$  and  $p_1$  as a function of  $\log_{10}(E)$  (see text) for EPOS-LHC as the hadronic interaction model. The dashed lines are the linear fits represented in Eq. (A.2).

A comparison between  $\log_{10} N_{\mu}^{\text{meas}}$  distributions achieved directly from CORSIKA showers and from the simulated method described in this work can be seen in Fig. A.3. The energy is fixed at  $E = 10^{19.0}$  eV and the hadronic interaction model is EPOS-LHC. The discrepancies in the mean values and in the  $\sigma$  of the distributions are less than 2% and 5% respectively, for any combination of primary and hadronic interaction model. Indeed, considering the differences between the approaches assumed by both software, CORSIKA and CONEX, these observed discrepancies are really satisfactory. Among the several physical effects which are treated differently we can highlight the lack of geomagnetic field and muon multiple scattering in CONEX.

Although there is a small discrepancy between our method's and CORSIKA's  $\log_{10} N_{\mu}^{\text{meas}}$  distributions, we do not expect to find any loss in the development of this paper. This can be assured because the method proposed here is not dependent on the comparison between our simulations and any other set of simulated showers.

**Table A1**  
Fitted parameters  $\alpha_0$ ,  $\beta_0$ ,  $\alpha_1$  and  $\beta_1$  given in Eq. (A.2).

Had. int. model	Primary	$\alpha_0$	$\beta_0$	$\alpha_1(10^{-5}g^{-1}cm^2)$	$\beta_1(10^{-5}g^{-1}cm^2)$
EPOS-LHC	proton	0.0303	-0.00635	-3.20	38.0
	helium	0.0385	-0.147	-4.14	53.6
	nitrogen	0.0337	-0.0721	-3.90	50.5
	iron	0.0259	0.0613	-3.04	35.8
QGSjetII-04	proton	0.0216	0.130	-2.04	17.3
	helium	0.0143	0.264	-1.20	1.35
	nitrogen	0.0167	0.209	-1.60	9.94
	iron	0.0245	0.0427	-2.99	38.5

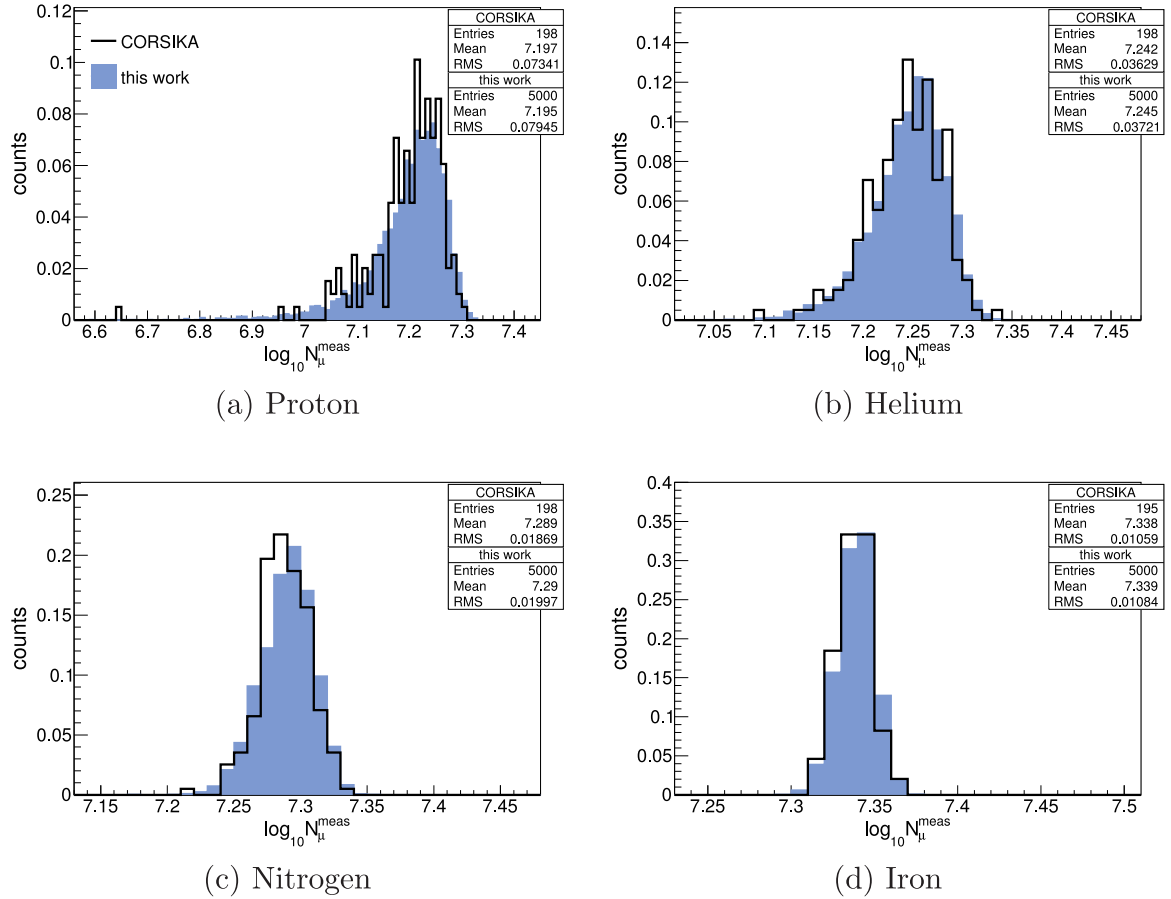


**Fig. A.3.** Comparison between the normalized  $\log_{10} N_{\mu}^{\text{meas}}$  distributions generated by CORSIKA and by this work's algorithm. The energy is  $E = 10^{19.0}$  eV and the hadronic interaction model is EPOS-LHC. The primary particles are (a) proton, (b) helium, (c) nitrogen and (d) iron.

## References

- [1] R. Abbasi (The HiRes Collaboration), Measurement of the flux of ultra high energy cosmic rays by the stereo technique, *Astropart. Phys.* 32 (1) (2010) 53–60. [10.1016/j.astropartphys.2009.06.001](https://doi.org/10.1016/j.astropartphys.2009.06.001).
- [2] J. Abraham (The Pierre Auger Collaboration), Measurement of the energy spectrum of cosmic rays above  $10^{18}$  eV using the Pierre Auger Observatory, *Phys. Lett. B* 685 (4–5) (2010) 239–246. [1002.1975](https://doi.org/10.1016/j.physletb.2010.02.013), doi:[10.1016/j.physletb.2010.02.013](https://doi.org/10.1016/j.physletb.2010.02.013).
- [3] A. Schulz, Measurement of the Energy Spectrum of Cosmic Rays above  $3 \times 10^{17}$  eV with the Pierre Auger Observatory, in: *Proceedings of the 33rd ICRC*, 2013.
- [4] T. Abu-Zayyad (The Telescope Array Collaboration), The cosmic-ray energy spectrum observed with the surface detector of the telescope array experiment, *Astrophys. J.* 768 (1) (2013) L1, doi:[10.1088/2041-8205/768/1/L1](https://doi.org/10.1088/2041-8205/768/1/L1).
- [5] D. Allard, et al., UHE nuclei propagation and the interpretation of the ankle in the cosmic-ray spectrum, *Astron. Astrophys.* 443 (2005) L29–L32. [astro-ph/0505566](https://doi.org/10.1051/0004-6361:200500199), doi:[10.1051/0004-6361:200500199](https://doi.org/10.1051/0004-6361:200500199).
- [6] V. Berezhinsky, A. Gazizov, S. Grigorjeva, On astrophysical solution to ultrahigh energy cosmic rays, *Phys. Rev. D* 74 (4) (2006) 043005, doi:[10.1103/PhysRevD.74.043005](https://doi.org/10.1103/PhysRevD.74.043005).
- [7] N. Globus, D. Allard, E. Parizot, A complete model of the CR spectrum and composition across the Galactic to Extragalactic transition, *Phys. Rev. D* 92 (2015) 021302(R). [1505.01377](https://doi.org/10.1103/PhysRevD.92.021302), doi:[10.1103/PhysRevD.92.021302](https://doi.org/10.1103/PhysRevD.92.021302).
- [8] V. Berezhinsky, A. Gazizov, S. Grigorjeva, Dip in UHECR spectrum as signature of proton interaction with CMB, *Phys. Lett. B* 612 (3–4) (2005) 147–153, doi:[10.1016/j.physletb.2005.02.058](https://doi.org/10.1016/j.physletb.2005.02.058).
- [9] P.L. Biermann, V. de Souza, Centaurus a: the extragalactic source of cosmic rays with energies above the knee, *Astrophys. J.* 746 (1) (2012) 72. [1106.0625](https://doi.org/10.1088/0004-637X/746/1/72), doi:[10.1088/0004-637X/746/1/72](https://doi.org/10.1088/0004-637X/746/1/72).
- [10] J. Abraham (The Pierre Auger Collaboration), *Phys. Rev. Lett.* 104 (9) (2010) 091101, doi:[10.1103/PhysRevLett.104.091101](https://doi.org/10.1103/PhysRevLett.104.091101).
- [11] A. Aab (The Pierre Auger Collaboration), Depth of maximum of air-shower profiles at the Pierre Auger Observatory. I. measurements at energies above  $10^{17.8}$  eV, *Phys. Rev. D* 90 (12) (2014) 122005, doi:[10.1103/PhysRevD.90.122005](https://doi.org/10.1103/PhysRevD.90.122005).
- [12] K.-H. Kampert, M. Unger, Measurements of the cosmic ray composition with air shower experiments, *Astropart. Phys.* 35 (10) (2012) 660–678. [1201.0018](https://doi.org/10.1016/j.astropartphys.2012.02.004), doi:[10.1016/j.astropartphys.2012.02.004](https://doi.org/10.1016/j.astropartphys.2012.02.004).
- [13] G.R. Farrar, The muon content of hybrid events recorded at the Pierre Auger Observatory, in: *Proceedings of the 33rd ICRC*, 2013.
- [14] A. Aab (The Pierre Auger Collaboration), Muons in air showers at the Pierre Auger Observatory: mean number in highly inclined events, *Phys. Rev. D* 91 (2015) 032003, doi:[10.1103/PhysRevD.91.032003](https://doi.org/10.1103/PhysRevD.91.032003).
- [15] D. Allard, E. Parizot, A.V. Olinto, On the transition from galactic to extragalactic cosmic-rays: spectral and composition features from two opposite scenarios, *Astropart. Phys.* 27 (1) (2007) 61–75. [astro-ph/0512345](https://doi.org/10.1016/j.astropartphys.2006.09.006), doi:[10.1016/j.astropartphys.2006.09.006](https://doi.org/10.1016/j.astropartphys.2006.09.006).
- [16] A. Aab (The Pierre Auger Collaboration), Depth of maximum of air-shower profiles at the Pierre Auger Observatory. II. composition implications, *Phys. Rev. D* 90 (12) (2014) 122006, doi:[10.1103/PhysRevD.90.122006](https://doi.org/10.1103/PhysRevD.90.122006).
- [17] J. Matthews, A Heitler model of extensive air showers, *Astropart. Phys.* 22 (5–6) (2005) 387–397, doi:[10.1016/j.astropartphys.2004.09.003](https://doi.org/10.1016/j.astropartphys.2004.09.003).
- [18] J. Alvarez-Muñiz, et al., Hybrid simulations of extensive air showers, *Phys. Rev. D* 66 (3) (2002) 033011. [astro-ph/0205302](https://doi.org/10.1103/PhysRevD.66.033011), doi:[10.1103/PhysRevD.66.033011](https://doi.org/10.1103/PhysRevD.66.033011).
- [19] A. Aab (The Pierre Auger Collaboration), *Nucl. Instrum. Meth. A* 798 (2015) 172–213, doi:[10.1016/j.nima.2015.06.058](https://doi.org/10.1016/j.nima.2015.06.058).
- [20] H. Kawai (The Telescope Array Collaboration), Telescope Array Experiment, *Nucl. Phys. B Proc. Suppl.* 175–176 (2008) 221–226, doi:[10.1016/j.nuclphysbps.2007.11.002](https://doi.org/10.1016/j.nuclphysbps.2007.11.002).
- [21] D. Heck, et al., CORSIKA: A Monte Carlo Code to Simulate Extensive Air Showers, Technical Report, Forschungszentrum Karlsruhe GmbH, Karlsruhe, 1998.
- [22] J.A. Ortiz, G. Medina-Tanco, V. de Souza, Longitudinal development of extensive air showers: hybrid code SENECA and full Monte Carlo, *Astropart. Phys.* 23 (5) (2005) 463–476. [astro-ph/0411421](https://doi.org/10.1016/j.astropartphys.2005.02.007), doi:[10.1016/j.astropartphys.2005.02.007](https://doi.org/10.1016/j.astropartphys.2005.02.007).
- [23] T. Bergmann, et al., One-dimensional hybrid approach to extensive air shower simulation, *Astropart. Phys.* 26 (6) (2007) 420–432, doi:[10.1016/j.astropartphys.2006.08.005](https://doi.org/10.1016/j.astropartphys.2006.08.005).
- [24] K. Werner, T. Pierog, Extended air shower simulations using EPOS, in: *AIP Conference Proceedings*, vol. 928, AIP, 2007, pp. 111–117, doi:[10.1063/1.2775903](https://doi.org/10.1063/1.2775903).
- [25] S. Ostapchenko, Monte Carlo treatment of hadronic interactions in enhanced Pomeron scheme: QGSJET-II model, *Phys. Rev. D* 83 (1) (2011) 014018. [1010.1869](https://doi.org/10.1103/PhysRevD.83.014018), doi:[10.1103/PhysRevD.83.014018](https://doi.org/10.1103/PhysRevD.83.014018).
- [26] J. Abraham (The Pierre Auger Collaboration), Trigger and aperture of the surface detector array of the Pierre Auger Observatory, *Nucl. Instrum. Meth. A* 613 (1) (2010) 29–39, doi:[10.1016/j.nima.2009.11.018](https://doi.org/10.1016/j.nima.2009.11.018).

- [27] J. Hersil, et al., Observations of extensive air showers near the maximum of their longitudinal development, *Phys. Rev. Lett.* 6 (1) (1961) 22–23, doi:[10.1103/PhysRevLett.6.22](https://doi.org/10.1103/PhysRevLett.6.22).
- [28] D.M. Edge, et al., The cosmic ray spectrum at energies above  $10^{17}$  eV, *J. Phys. A* 6 (1973) 1612, doi:[10.1088/0305-4470/6/10/019](https://doi.org/10.1088/0305-4470/6/10/019).
- [29] M. Nagano, et al., Energy spectrum of primary cosmic rays between  $10^{14.5}$  and  $10^{18}$  eV, *J. Phys. G* 10 (1984) 1295–1310, doi:[10.1088/0954-3889/18/2/022](https://doi.org/10.1088/0954-3889/18/2/022).
- [30] C. Di Giulio, Energy calibration of data recorded with the surface detectors of the Pierre Auger Observatory, in: *Proceedings of the 31st ICRC, Łódź, Poland, 2009*.
- [31] W.D. Apel (The KASCADE-Grande Collaboration), Cosmic ray energy reconstruction from the S(500) observable recorded in the KASCADE-grande air shower experiment, *Astropart. Phys.* 77 (2016) 21–31, doi:[10.1016/j.astropartphys.2015.12.002](https://doi.org/10.1016/j.astropartphys.2015.12.002).
- [32] J.C. Arteaga-Velazquez, The energy spectrum of primary cosmic rays reconstructed with the KASCADE-grande muon data, in: *Proceedings of the 31st ICRC, Łódź, Poland, 2009*.
- [33] H. Sagawa, Telescope array extension: TA x 4, in: *Proceedings of the 34th ICRC, 2015*.
- [34] R. Engel, Upgrade of the Pierre Auger Observatory (AugerPrime), in: *Proceedings of the 34th ICRC, 2015*.
- [35] G. Battistoni, et al., The FLUKA code: description and benchmarking, in: *AIP Conference Proceedings*, vol. 896, 2007, pp. 31–49.